



Coseismic and Pre-seismic Deformation Characteristics of the 2022 M_S 6.9 Menyuan Earthquake, China

NANNAN GUO,¹ YANQIANG WU,¹  and QINGYUN ZHANG¹

Abstract—On January 8, 2022, the M_S 6.9 Menyuan earthquake occurred in Menyuan, Qinghai province, China; the epicenter was on the fault terrace of the Lenglongling and Tuolaishan faults. To investigate the coseismic and pre-seismic deformation associated with the event, we constructed physical models using interferometric synthetic aperture radar (InSAR) and global navigation satellite system (GNSS) data and inverted the fault slip distribution, fault coupling fraction, fault slip deficit and strain rate. The primary inversion results were as follows: (1) The InSAR coseismic deformation pattern indicates that the left-lateral strike-slip deformation occurred in the NW–SE direction, with the maximum relative displacement in the line-of-sight direction being 1.3 m. (2) The coseismic slip mainly occurred in a 30×25 km region at a depth of 0–8 km. The maximum fault slip was 3.81 m with a moment magnitude (M_W) of 6.6. (3) Based on the fault coupling inversion, the seismogenic fault was strongly locked (> 0.96) up to a depth of ~ 10 km before the Menyuan earthquake. The coseismic rupture zone in the fault strike direction was significantly smaller than the pre-seismic locked region. (4) The pre-seismic strain rates revealed NE–SW compressive and NW–SE tensile deformations, reflecting a considerable left-lateral strain accumulation in the seismogenic region, with a maximum shear strain rate of 2.6×10^{-8} /year. Therefore, attention must be paid to the seismic hazards posed by the Tuolaishan and Lenglongling faults adjacent to the seismogenic region.

Keywords: Coseismic deformation, fault slip distribution, fault coupling fraction, pre-seismic deformation, GNSS.

1. Introduction

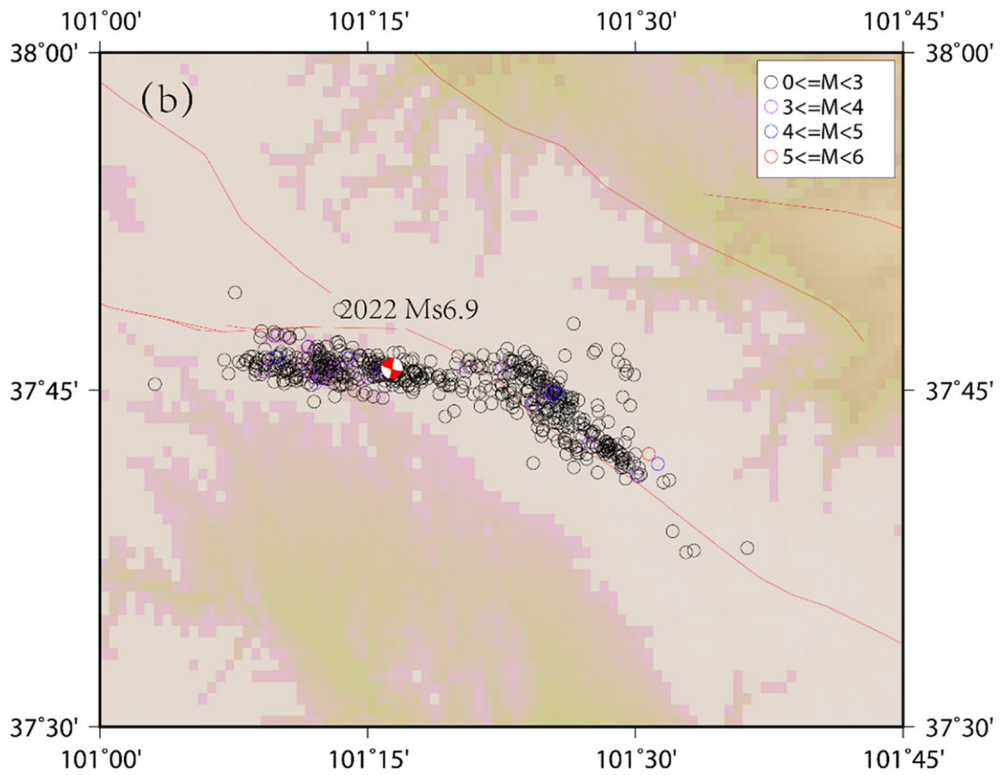
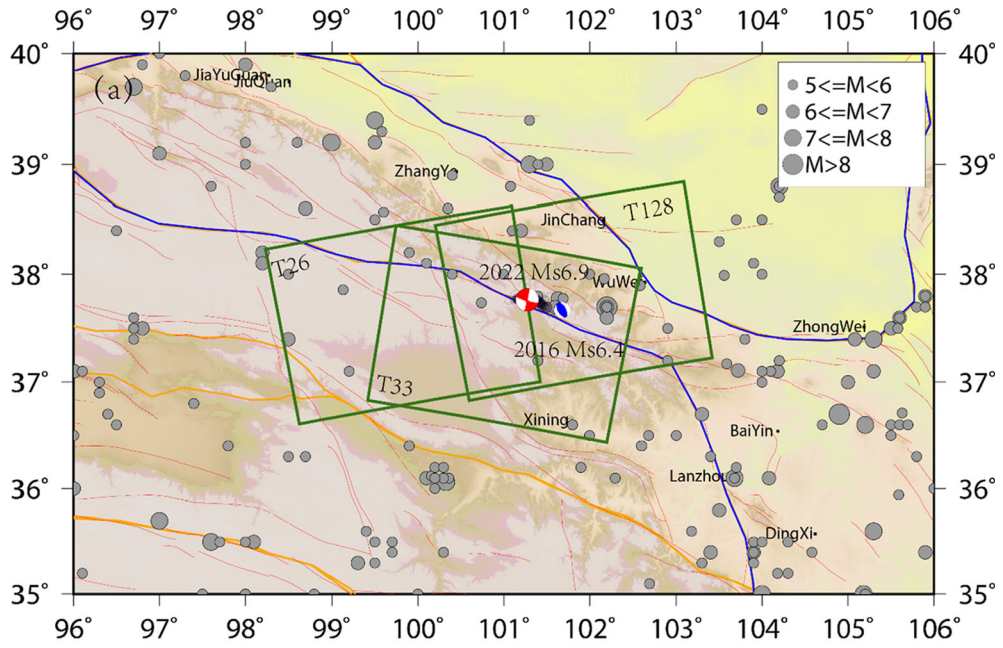
On January 8, 2022, an M_S 6.9 earthquake struck Menyuan County in Qinghai province, China, ~ 32 km west of the location of the 2016 M_S 6.4 Menyuan earthquake in the Qilianshan seismic belt. The epicenter was close to the northern Tuolaishan fault at

the northeastern margin of the Tibetan Plateau (Fig. 1). According to the Earthquake Networks Center (CENC), the epicenter of the earthquake was at 37.77° N, 101.26° E (CENC, 2022). The strike and dip values of the two nodal planes obtained by the US Geological Survey (USGS) were $104^\circ/88^\circ$ and $13^\circ/75^\circ$ (USGS, 2022), and the cumulative seismic moment release was M_W 6.6.

The 2022 M_S 6.9 Menyuan earthquake occurred in the northeastern margin of the Tibetan Plateau, which is tectonically complex because of the intense NE compression of the Tibetan Plateau, induced by the NE compression of the Indian Plate (Guo et al., 2017; He et al., 2000; Li et al., 2016a). The Qilianshan seismic belt is characterized by complex tectonic setting, including NE shortening, dextral rotation and SE compression (Yuan et al., 2004). Historical seismic data also reveal a complex seismotectonic setting in the region. Many earthquakes with magnitudes > 7.0 have occurred in the region, including the 1920 M_S 8.5 Haiyuan, 1927 M_S 8.0 Gulang and 1954 M_S 7.2 Shandan earthquakes (Fig. 1). The most recent earthquake of magnitude > 6.0 in the region was the 2016 M_S 6.4 Menyuan earthquake, which was a thrust earthquake with left-lateral strike-slip components (Wang et al., 2017) associated with the northern Lenglongling Fault (Hu et al., 2016; Li et al., 2017). The epicenters of the 2022 M_S 6.9 and 2016 M_S 6.4 earthquakes were only 32 km apart; however, the seismogenic mechanisms underlying the two were different events.

The slip model of the 2022 Menyuan earthquake shows that it created a 20-km-long surface rupture (Yang et al., 2022). Based on the interferometric synthetic aperture radar (InSAR)-derived coseismic deformation fields and optical remote sensing images,

¹ The First Monitoring and Application Center, China Earthquake Administration, Tianjin 300180, China. E-mail: chdqyw@126.com



◀Figure 1

Geologic map of the 2022 M_S 6.9 Menyuan earthquake region. **a** $M > 5.0$ earthquakes are indicated by solid gray circles. Red and blue beachballs represent the focal mechanism solutions of the 2022 M_S 6.9 and 2016 M_S 6.4 Menyuan earthquakes, respectively. Red lines represent major faults, while blue and yellow lines represent block boundaries. Dark green rectangle indicates interferometric synthetic aperture radar (InSAR) observation coverage. Black solid squares indicate major cities in the region. **b** Black circles indicate the aftershock locations of the 2022 Menyuan earthquake (Fan et al., 2022)

Li et al. (2022) observed that the northwestern segment of the Lenglongling fault caused the 2022 earthquake; the rupture extended west to the Tuolaishan fault. Previous studies have focused on the coseismic deformation characteristics and the fault slip model of the 2022 Menyuan earthquake but have not explored the pre-seismic characteristics of the seismogenic faults and the relationship between coseismic and pre-seismic deformation characteristics. In addition, this study introduces more InSAR observation to invert the coseismic deformation field of this earthquake, which provides robust data constraints. We also analyze the pre-seismic characteristics of the seismogenic fault, such as the coupling fraction, slip deficit rate and strain accumulation, while previous studies have not estimated such characteristics. Investigating the pre-seismic and coseismic deformations in the region could provide insights into the seismic deformation processes, earthquake mechanisms and potential seismic hazards. Our results could facilitate subsequent research and provide further insights into the seismogenic mechanism, which may enhance our understanding of the seismic hazards of adjacent faults.

2. Coseismic Deformation and Fault Slip Inversion

Geodetic techniques have been used to investigate the coseismic deformation and focal mechanisms of earthquakes (Wang et al., 2017; Wu et al., 2016). Because of its high spatial resolution, InSAR technology is effective for determining the coseismic displacement fields of large earthquakes and inverting for the geometric distribution of seismic faults (Ji

et al., 2017; Qu et al., 2013; Shan et al., 2017; Wang et al., 2007).

2.1. InSAR Coseismic Deformation

The Sentinel-1 satellite, launched by the European Space Agency (ESA) on April 3, 2014, has a short (12 days) revisit period (6 days for Sentinel-1B). After the 2022 M_S 6.9 Menyuan earthquake, the ESA obtained Sentinel-1 Interferometric Wide images from the ascending and descending orbits. The ascending/descending track InSAR observations (Table 1) were processed using the GMT5SAR program (Sandwell et al., 2011; Xu et al., 2017). The SRTM3 digital elevation model, which has a resolution of three arc-second (90 m), was used to remove the topographic phase. An 10×2 multi-look ratio was configured for the Sentinel-1 interferograms to minimize speckle noise, and interferogram smoothing was performed using a 200-m Gaussian filter. The unwrapping procedure was implemented using the Statistical-Cost Network-Flow Algorithm for Phase Unwrapping software package (Chen & Zebker, 2001). The InSAR coseismic deformation fields from the ascending/descending orbits were obtained by geocoding the deformation maps to convert the radar coordinates into geographic coordinates (Fig. 2).

The deformation maps derived from the InSAR data from the ascending and descending orbits showed a butterfly-like pattern (Fig. 2). The derived coseismic displacement fields exhibited opposite trends on both sides of the causative fault, indicating that the fault is dominated by a horizontal motion. Combined with the relationship between the uplift and subsidence in the line-of-sight (LOS) direction of the difference tracks, it can be interpreted that the deformation was caused by the left-lateral strike-slip movement of the fault. These results indicated that the 2022 Menyuan earthquake was a left-lateral strike-slip rupture. The coseismic deformation field indicated that the rupture occurred in the NWW-SEE direction, which is consistent with the earthquake aftershock distribution (Fan et al., 2022). The maximum coseismic displacements in the LOS direction were ~ 66 and 72 cm along the ascending track and ~ 75 cm along the descending orbit; thus, the

Table 1
Detailed interferogram information

Satellite	Track no	Flight direction	Wavelength (cm)	Master image	Slave image	Temporal baseline (days)
Sentinel-1A	T26	Ascending	5.6	20211229	20220110	12
Sentinel-1A	T128	Ascending	5.6	20220105	20220117	12
Sentinel-1A	T33	Descending	5.6	20211229	20220110	12

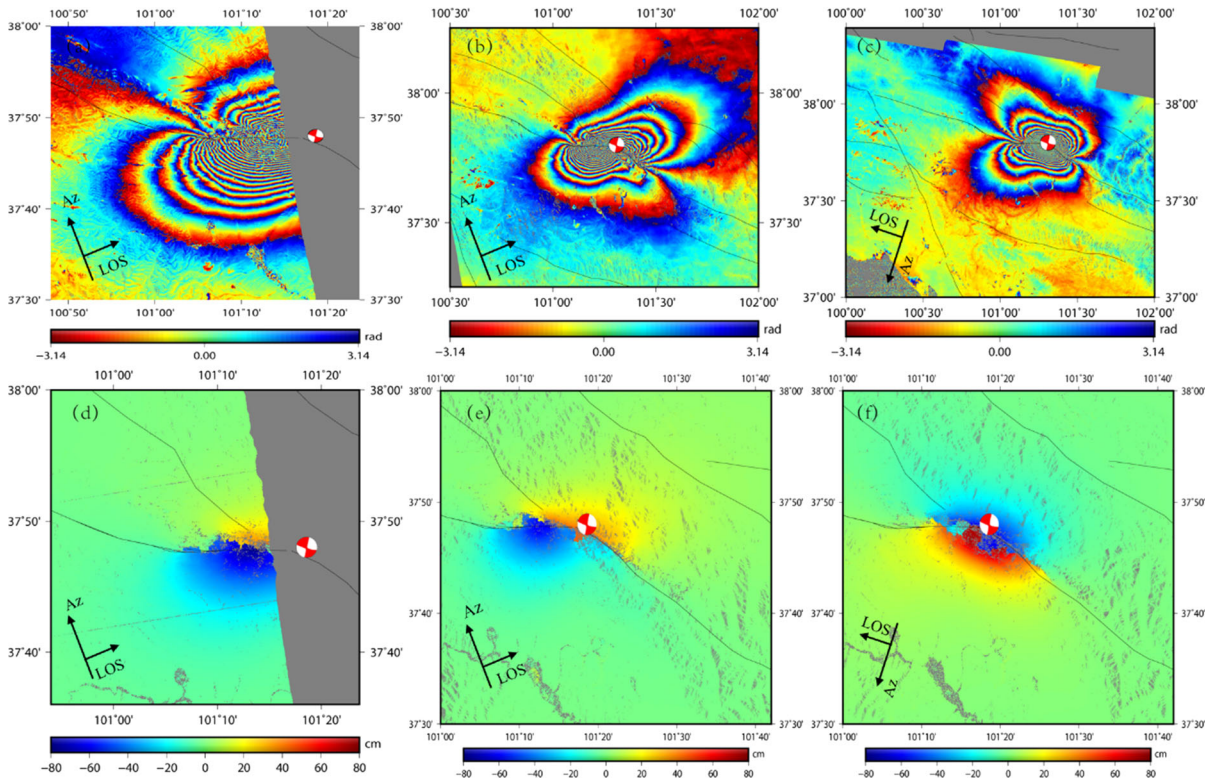


Figure 2

InSAR coseismic deformation field of the 2022 M_S 6.9 Menyuan earthquake. Coseismic interferometric phase from **a** the T26 ascending track, **b** T128 ascending track and **c** T33 descending track. Coseismic deformation field from **d** the T26 ascending track, **e** T128 ascending track and **f** T33 descending track

maximum relative displacement in the LOS was ~ 1.3 m. The deformation field of the 2022 Menyuan earthquake was $\sim 30 \times 25$ km wide (deformations > 10 cm are labeled in Fig. 3b and c with blue rectangle). More deformation occurred on the southern side of the fault than on the northern side. Because of the surface rupture generated by the earthquake, near-field deformation was large, which led to decoherence near the fault. Therefore, these local deformation signals were not measured.

2.2. Coseismic Fault Slip Inversion

A preliminary field survey by Yuan (2022) observed that the 2022 Menyuan earthquake generated significant surface rupture (> 22 km) comprising two distinct rupture zones. The primary rupture on the northern side propagated NWW along the western segment of the Lenglongling fault, whereas the secondary rupture on the southern side occurred on the eastern segment of the Tuolaishan fault and propagated nearly EW, with a length

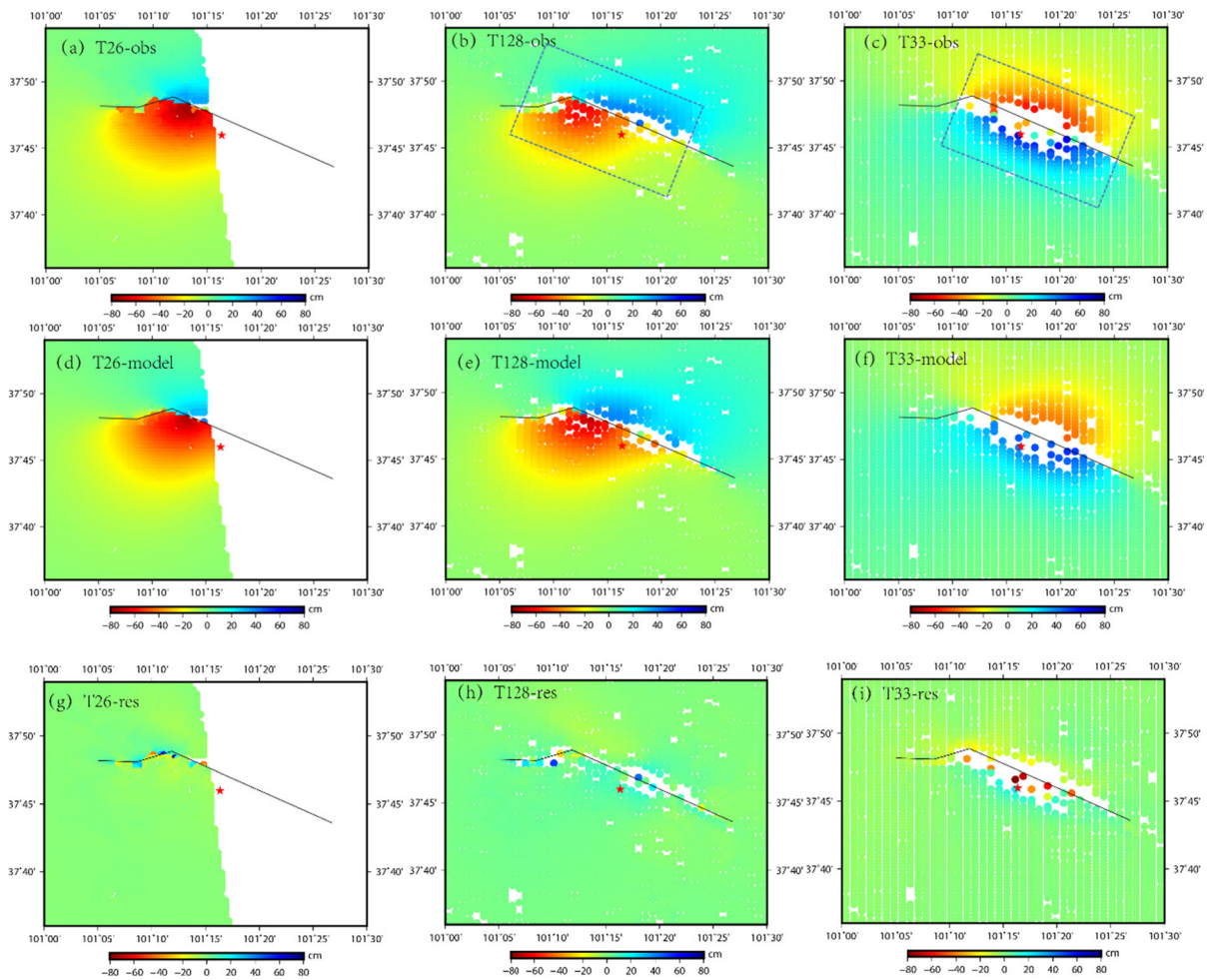


Figure 3

Observed InSAR deformation field, simulated deformation field and the residuals. **a–c** Observed deformation fields for tracks T26, T128 and T33, respectively; **d–f** simulated deformation fields for tracks T26, T128 and T33, respectively; **g–i** deformation residuals for tracks T26, T128 and T33, respectively

of ~ 5 km, and was characterized by horizontal dislocations ranging from 0.5 to 0.9 m. The secondary rupture and western segment of the primary rupture formed a pair of left-stepping echelon faults, which correspond to the termination of the westward propagation of the 2022 earthquake rupture. Two rupture segments have been reported for this earthquake; therefore, we used two fault segments for the inversion.

To determine the rupture mechanism and fault slip of the 2022 Menyuan earthquake, we created an inversion model for the fault slip using the steepest descent method (Wang et al., 2008) based on the

Okada's dislocation model (Okada, 1992). First, the fault geometry was modeled using the focal mechanism solutions obtained from the US Geological Survey (USGS, 2022) and Global Centroid Moment Tensor catalog (GCMT, 2022) (Table 2). Next, the fault model was characterized using the InSAR coseismic deformation fields obtained from the three satellite orbits and inverted for the fault slip of two fault segments. To generate a precise fault slip model, the fault was divided into 1×1 km sub-faults with boundary point coordinates of 37.72°N , 101.43°E and 37.80°N , 101.11°E . Because of the complexity of the causative fault, the fault dip range was set to

Table 2
Focal mechanism solutions of the 2022 Menyuan earthquake

Source	Epicenter		Focal depth (km)	Magnitude (M_w)	Nodal planes I and II		
	Latitude ($^{\circ}$)	Longitude ($^{\circ}$)			Strike ($^{\circ}$)	Dip ($^{\circ}$)	Rake ($^{\circ}$)
USGS	37.815	101.278	13.0	6.6	13	75	178
					104	88	15
GCMT	37.80	101.31	14.8	6.7	14	89	172
					104	82	1

GCMT Global Centroid Moment Tensor, USGS US Geological Survey

70° – 90° . The length and width of the fault area were set to 30 km and 20 km, respectively, and the maximum slip was 10 m. The fault strike was estimated during inversion. With the trade-off curve between the dislocation model roughness and the data fitting degree, the smoothing factor for the inversion was set to $\alpha = 0.15$. The InSAR data of the three tracks were assigned equal weight. Finally, uniformly down-sampled InSAR coseismic deformation fields were simultaneously inverted. Figure 3 illustrates the coseismic deformation fields obtained from the down-sampled InSAR deformation fields and model values derived from the simulation. The simulated InSAR coseismic deformation field was highly correlated (fit 0.97) with the observed values, and the deformation residuals in different tracks were small. To quantify the reliability of the model, the root-mean-square (RMS) errors were computed. Overall residuals of 3.2 cm, 1.8 cm and 3.3 cm were obtained

for the ascending T26, ascending T128 and descending T33 tracks, respectively.

We obtained an inversion model for the fault slip from the InSAR observations. Figure 4 illustrates the fault slip distribution. The maximum coseismic slip of 3.81 m occurred at 37.78° N and 101.27° E at a depth of 3.5 km. The model indicated a seismic moment corresponding to M_w 6.6, which is consistent with the seismic parameters obtained from USGS and GCMT. The fault slip occurred on the ~ 24 -km-long primary rupture (S1) oriented in the NWW direction. At a depth of 0–8 km, the S1 slip varied between 2 and 3.8 m with an approximately elliptical distribution around a maximum slip of ~ 3.81 m. The slip magnitude gradually decreased eastward and westward from S1. At depths > 10 km, the slip was almost zero. The secondary rupture (S2), which was ~ 6 km long, oriented near EW; its maximum slip (~ 0.94 m) occurred at a depth of 3 km, ranging

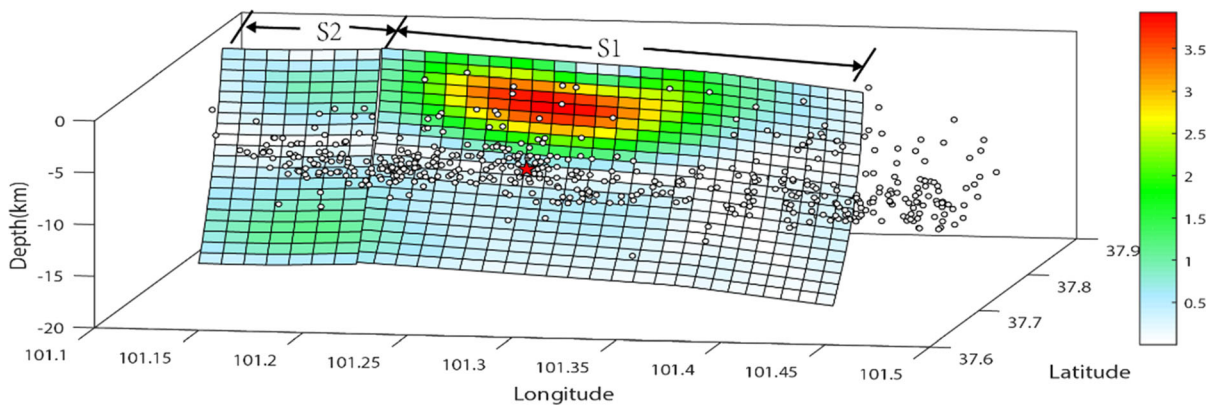


Figure 4

Fault slip model. White circles indicate precise aftershock locations (Fan et al., 2022), and the red star indicates the epicenter of the 2022 Menyuan earthquake

from 0.5 to 0.9 m. The terminal points of S2 exhibited some degree of compression. In the fault model of S1, most of the slip occurred at depths shallower than 10 km, which was close to the lower boundary of the aftershock depth distribution. The inversion model indicates that the fault dipped towards the south. High-precision aftershock location data also indicated that the aftershocks primarily occurred on the southern side of the rupture area (Fan et al., 2022). The InSAR coseismic deformation fields suggest asymmetric deformations on the southern and northern sides of the seismogenic fault; the southern side underwent larger deformation compared to the northern side.

3. Pre-seismic Fault Coupling and Deformation Feature

Because coseismic stress and strain accumulated prior to and are released during an earthquake, pre-seismic crustal deformation could provide important insights into the seismogenic mechanisms. To examine the characteristics of pre-seismic deformation associated with the Menyuan earthquake, we

investigated the fault coupling distribution, fault slip deficit and strain accumulation using GNSS data.

3.1. Fault Coupling Inversion

The inversion of geodetic data, such as GNSS data, to obtain fault locking and slip deficit can help to estimate seismic fault hazards (Li et al., 2017; Zhao et al., 2020). Inversion modeling for pre-seismic fault coupling may also provide information on the seismogenesis of the 2022 Menyuan earthquake. We used the DEFNODE program (McCaffrey, 2005) to estimate the fault coupling state using the GNSS velocity field by Wang and Shen (2020), who compiled ~ 20 years of GNSS data. Figure 5 shows the GNSS velocity field in the study area. To obtain the deformation of the seismogenic fault and adjacent area, the fault was divided into two active blocks, namely the Gansu and Qilian blocks (Li et al., 2014; Wang et al., 2011). The fault trace for the inversion is shown in Fig. 5 as a bold and dark green line, which is located along the Lenglongling and Tuolaishan faults.

Figure 6 shows the depth-dependent fault coupling distribution along the seismogenic fault, which

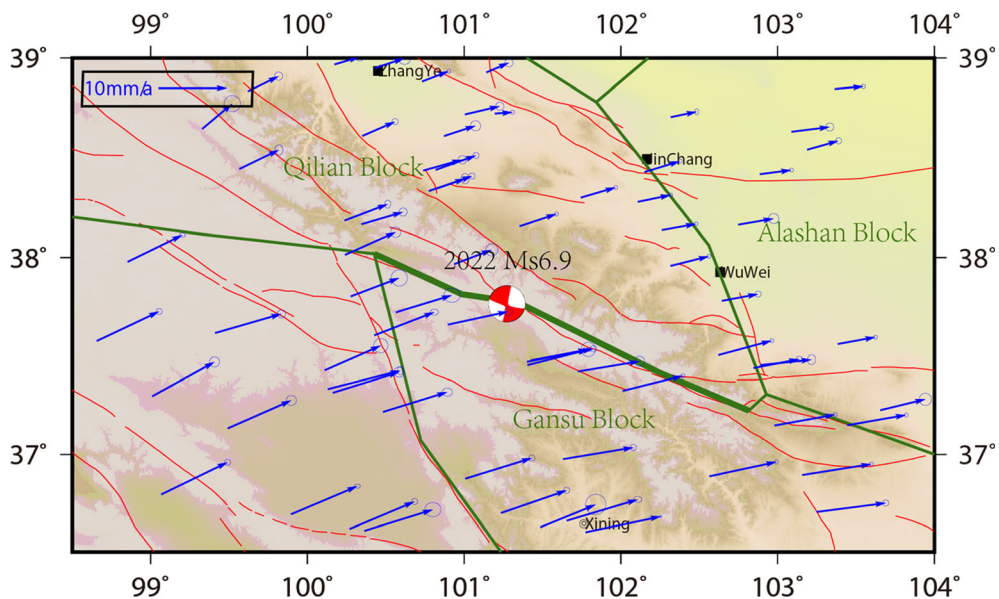


Figure 5

GNSS velocity field and inversion model block divisions. Blue arrows represent the GNSS velocity field, and the dark green lines represent the active block boundaries. The bold and dark green line is the inversion fault

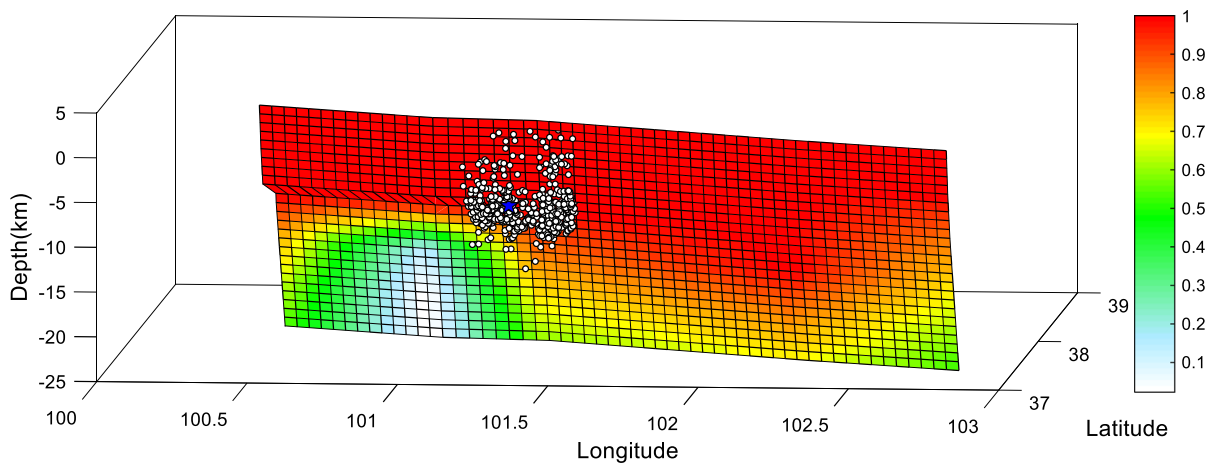


Figure 6

The fault coupling distribution of the seismogenic fault. White circles indicate precise seismic locations (Yang et al., 2022), and the blue star indicates the epicenter of the 2022 Menyuan earthquake

indicates a high degree of fault coupling and locked depth. The result shows that the seismogenic fault of the 2022 Menyuan earthquake was strongly coupled (coupling coefficient > 0.96) at a depth of 0–10 km. The coseismic rupture zone strongly correlated with the pre-seismic locked zone. However, the coseismic rupture zone along the fault strike was considerably smaller than the coupled zone. In addition, the eastern part of the fault was more strongly coupled than the western part.

To evaluate the inversion results, we estimated the mismatched value of the parameter fitting and the residuals of the GNSS velocity field. In the inversion of GPS horizontal velocity field to obtain parameters, such as block rotation, uniform strain inside the block and fault locking, the mismatched values of parameter fitting can be represented as follows (McCaffrey, 2002; Li et al., 2016b; Zhao et al., 2020):

$$\chi_n^2 = \left[\sum_{i=1}^n (r_i/f\sigma_i)^2 \right] / \text{dof}, \quad (1)$$

where r_i is the residual, σ_i is the standard deviation, and dof is the degrees of freedom (McCaffrey, 2002). The range of the uncertainty scaling factor, f , of the GPS horizontal velocity field is generally 1–5 (Mao et al., 1999). We achieved $\chi_n^2 = 1.007$ by constantly changing f , and the model explained the observation well. Moreover, we analyzed the GNSS velocity

residuals (Fig. 7) and found the residuals were relatively small; a few residuals in the Qilian block far from the fault were slightly larger.

3.2. Fault Slip Deficit

The fault locking reflects the ability of the fault to accumulate strain; the stronger the fault coupling is, the higher the strain accumulation. The fault strain accumulation rate needs to be quantitatively described by the slip deficit rates. The slip deficit is the product of the long-term fault slip rate and the fault locking coefficient. Figure 8 shows the distribution of the fault-parallel slip deficit rate, which corresponds to the shear strain accumulation rate in the fault zone. The obtained fault-parallel slip deficit rate was higher over depths of 0–10 km; the average rate was 4.7 mm/year, indicating faster strain accumulation. Furthermore, the shear strain accumulation rate in the fault zone was higher than that in the surrounding area, which points toward the seismic hazard of this area.

3.3. Strain Rate Distribution

The GNSS strain rate fields can reflect the strain accumulation before an earthquake as well as the pregnancy characteristics (Wu et al., 2013, 2016, 2021). Variations in the regional crustal

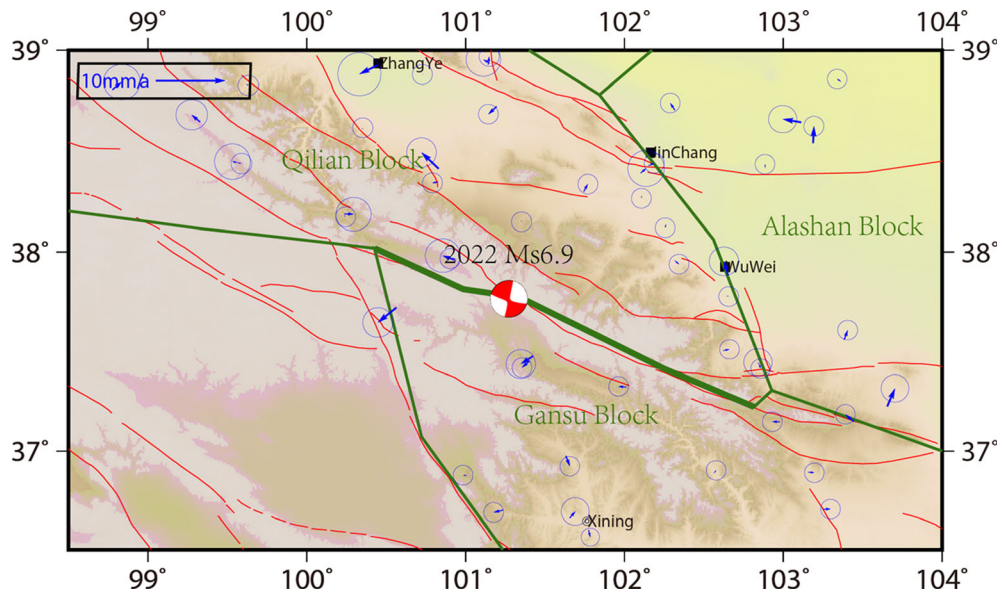


Figure 7

Distribution of GNSS velocity residuals. Blue arrows represent the GNSS velocity residuals, while dark green lines represent the active block boundaries. The bold dark green line is the inversion fault

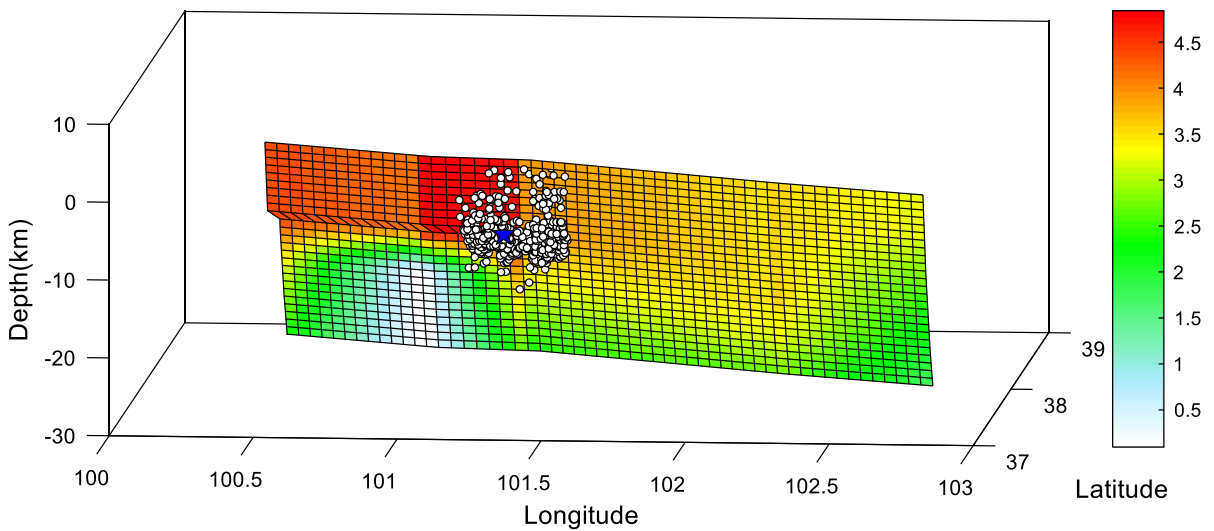


Figure 8

Spatial characteristics of fault-parallel slip deficit rates in the seismogenic fault

deformation before an earthquake provide insights for estimating the risks of large future earthquakes in an area.

To investigate the strain accumulation in the 2022 Menyuan earthquake source location, we determined the strain rate using the least-squares collocation

method (Wu et al., 2009, 2011). The surface strain rates are given in Fig. 9a, showing that the compressive deformation was predominant at the epicenter region because of the NE expansion of the Tibetan Plateau. The principal strain rates indicate NE–SW compressive and NW–SE tensile deformation with

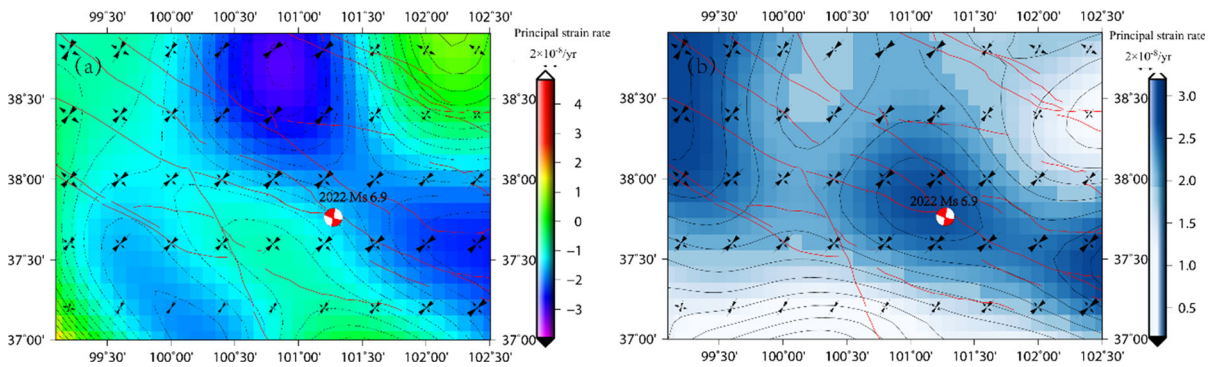


Figure 9
a Surface and principal strain rates. **b** Maximum shear and principal strain rates

average values of -3.0×10^{-8} /year and 1.8×10^{-8} /year, respectively. The strain rates reflect large strain accumulation with left-lateral strike-slip component in the seismogenic region. The greatest shear strain rate (maximum of 2.6×10^{-8} /year) was observed near the 2022 Menyuan earthquake epicenter (Fig. 9b).

4. Discussion

4.1. Reliability Analysis of Coseismic Fault Slip Model

We obtained ascending and descending InSAR coseismic deformation data from three satellite orbits to investigate the characteristics of coseismic deformation. To confirm the reliability of the inversion results, we analyzed the residuals of the fault slip inversion and found that the residuals were relatively small and mostly concentrated near the fault, whereas the far-field residuals were almost zero. Overall, the simulated results were highly correlated with the observations ($R^2 = 0.97$). The root-mean-square values of residuals between the InSAR observations and simulations were 2–3 cm; hence, the physical model could explain the observations well.

The seismogenic mechanism results and fault slip model from this paper were consistent with previous findings (Li et al., 2022; Peng et al., 2022; Yang et al., 2022). The primary fault segment (rupture length > 20 km) was oriented in the NWW direction, which is consistent with the findings of field surveys

(22 km of rupture). The main slip was concentrated over depths of 0–8 km with a maximum slip of ~ 3.81 m, which is greater than the reported maximum slip of ~ 3.5 m (Li et al., 2022; Yang et al., 2022). This difference may be attributed to the addition of the InSAR coseismic deformation field of ascending track in our model, which covers the complete deformation region. The ~ 6 km long secondary fault segment was oriented in the near EW direction and had a slip of 0.5–0.9 m (Fig. 4), with an average slip of ~ 0.3 m, consistent with the results reported by Yang et al. (2022). In general, our fault slip model is consistent with the existing slip distribution (Li et al., 2022; Yang et al., 2022).

4.2. Coseismic Deformation Characteristics of Seismogenic Faults

The InSAR coseismic deformation fields and inversion results estimated in the present study exhibited asymmetric deformation on the southern and northern sides of the seismogenic faults. A higher deformation was observed on the southern side than on the northern side, which is attributed to three possible reasons. First, the Menyuan M_S 6.9 earthquake occurred at the northeastern margin of the Tibetan Plateau, where a left-lateral strike-slip fault was formed because of the NE compressive shortening and SEE tensile deformation. The coseismic deformation, affected by the crustal density and structure in the region, was conducive to earthquake and lateral flow of crustal material (Wang et al.,

2013). Second, the media parameters on the northern and southern sides of the seismogenic faults differed (Wang et al., 2013, 2016); the southern side was more prone to deformation. Third, the inverted fault slip model dipped southward, which may explain the NS asymmetry of the fault deformation.

4.3. Relationship Between Pre-seismic Deformation Characteristics and Seismogenic Faults

In the present study, the strain accumulation, coupling state and slip deficit of the seismogenic fault before the 2022 Menyuan earthquake were estimated. The obtained fault coupling fraction indicated that the seismogenic portion of the fault was highly locked at depths of 0–10 km (Fig. 6). The average of the fault-parallel slip deficit rate was ~ 4.7 mm/year (Fig. 8), consistent with previous findings (Li et al., 2016b; Zhao et al., 2016). Results showed that the 2022 earthquake occurred in the region of strongly coupled and high slip deficit rate, which indicates that the strain accumulated quickly before the fault rupture. Large earthquakes were prone to occur when faults are strongly coupled and the accumulation of strain energy along the fault is high. It is consistent with the conclusion that many large earthquakes occur in the strong-locked region or near the strong-weak-locked high gradient zone (Avouac et al., 2015; Loveless & Meade, 2011; Moreno et al., 2010; Schurr et al., 2014; Wu et al., 2015; Zhao et al., 2020).

The strain rate distribution near the 2022 Menyuan earthquake was characterized as NE–SW compression and NW–SE extension. The average compression and extension rates were -3.0×10^{-8} /year and 1.8×10^{-8} /year, respectively (Fig. 9), consistent with the results of Gan et al. (2007), Ge et al. (2015) and Chen et al. (2017). The strain rate distribution shows that the earthquake occurred in a region where high shear strain was accumulated, indicating that the strain energy of the seismogenic fault accumulated faster. The results are consistent with the conclusion of Wu et al. (2021), showing that majority ($> 76.9\%$) of earthquakes with $M > 6.5$ occur in the region with a high-strain rate. However, because the GNSS data are sparse, localized features could not be reflected in the inverse modeling for estimating the fault locking and strain rate.

Meanwhile, this earthquake was located in the seismic gap of the Qilian-Haiyuan fault zone (Tianzhu seismic gap) (Gaudemer et al., 1995) and could accumulate higher stress and strain; therefore, it had a strong earthquake risk, which promoted the 2022 Menyuan earthquake. Furthermore, the Lenglongling-Tuolaishan fault in the western section of the Qilian-Haiyuan fault remains strongly coupled and continues to accumulate strain energy, so that seismic risks in the regions remain high. This highlights the importance of monitoring the Lenglongling and Tuolaishan faults because of their seismic potential.

5. Conclusion

Deformation associated with the 2022 M_S 6.9 Menyuan earthquake primarily occurred within a 30×25 km region at depths of 0–8 km and the maximum line-of-sight displacement was of 1.3 m. The deformation fields on the northern and southern sides of the fault were asymmetric; deformation was slightly higher on the southern side than on the northern side. The maximum slip on the fault surface was ~ 3.81 m, and the moment magnitude of the earthquake was M_W 6.6. The pre-seismic GNSS data indicated that the seismogenic fault was highly locked at depths of 0–10 km, which corresponds with the location of the coseismic rupture zone. The strain rates indicate that the epicenter was in a left-lateral compressive deformation region. The maximum rate of shear strain of the epicentral area was 2.6×10^{-8} /year. The coseismic deformation was highly correlated with the fault locking and strain accumulation; however, rupture in the coseismic zone was substantially smaller than that in the locked zone. Therefore, close attention must be paid to the seismic hazards posed by the Tuolaishan and Lenglongling faults adjacent to the seismogenic structure in the future. Our results provide insights into the coseismic and pre-seismic deformation of the seismogenic fault associated with the 2022 Menyuan earthquake and will facilitate subsequent studies on the seismogenic mechanisms of large earthquakes and seismic forecasting.

Acknowledgements

The authors are grateful to the editor and two anonymous reviewers for their constructive comments on our manuscript. Thanks a lot for the helpful advice from Jing Zhao (China Earthquake Networks Center) and Qiang Li (Fujian Earthquake Agency). The authors would also like to thank the European Space Agency (ESA) for providing the Sentinel-1 data. We used the GMT5SAR software to generate InSAR data. This work was supported by the National Key R&D Program of China (grant number 2017YFC1500501); National Natural Science Foundation of China (grant nos. 41974011); Science and Technology Innovation Fund of the First Monitoring and Application Center, China Earthquake Administration (grant no. FMC2022002); Scientific Research Project Coordinating Fund of the First Monitoring and Application Center, China Earthquake Administration (grant no. FMC2022016).

Author Contributions NG: writing—review and editing. YW: conceptualization, methodology. QZ: validation.

Declarations

Conflict of Interest The authors declare that they have no known competing financial interests or personal relationships that could have appeared to influence the work reported in this paper.

Publisher's Note Springer Nature remains neutral with regard to jurisdictional claims in published maps and institutional affiliations.

Springer Nature or its licensor holds exclusive rights to this article under a publishing agreement with the author(s) or other rightsholder(s); author self-archiving of the accepted manuscript version of this article is solely governed by the terms of such publishing agreement and applicable law.

REFERENCES

- Avouac, J. P., Meng, L. S., Wei, S. J., Wang, T., & Ampuero, J. P. (2015). Lower edge of locked Main Himalayan Thrust unzipped by the 2015 Gorkha earthquake. *Nature Geoscience*, 8, 708–711.
- Chen, C. W. (2001). *Statistical-cost network-flow approaches to two-dimensional phase unwrapping for radar interferometry*. Stanford University.
- Chen, W. T., Gan, W. J., & Xiao, G. R. (2017). The regional crustal deformation before the 2016 Menyuan $M_s6.4$ earthquake. *Journal of Geodesy and Geodynamics*, 37(8), 777–781.
- China Earthquake Networks Center, (2022). <https://www.cenc.ac.cn/cenc/dzxx/396391/index.html>
- Fan, L. P., Li, B. R., Liao, S. R., Jiang, C., & Fang, L. H. (2022). High-precision relocation of the aftershock sequence of the January 8, 2022, $M_s6.9$ Menyuan earthquake. *Earthquake Science*. <https://doi.org/10.1016/j.eqs.2022.01.021>
- Gan, W. J., Zhang, P. Z., Shen, Z. K., Niu, Z. J., Wang, M., Wan, Y., Zhou, D. M., & Cheng, J. (2007). Present-day crustal motion within the Tibetan Plateau inferred from GPS measurements. *Journal of Geophysical Research*. <https://doi.org/10.1029/2005JB004120>
- Gaudemer, Y., Tapponnier, P., Meyer, B., Peltzer, G., Guo, S. M., Chen, Z. T., Dai, H., & Cifuentes, I. (1995). Partitioning of crustal slip between linked, active faults in the eastern Qilian Shan, and evidence for a major seismic gap, the 'Tianzhu gap', on the western Haiyuan Fault, Gansu (China). *Geophysical Journal International*, 120(3), 599–645.
- Ge, W. P., Molnar, P., Shen, Z. K., & Li, Q. (2015). Present-day crustal thinning in the southern and northern Tibetan Plateau revealed by GPS measurements. *Geophysical Research Letters*, 42(13), 5227–5235.
- Guo, P., Han, Z. J., An, Y. F., Jiang, W. L., Mao, Z. B., & Feng, W. (2017). Activity of the Lenglongling fault system and seismotectonics of the 2016 $M_s6.4$ Menyuan earthquake. *Science China Earth Sciences*, 47(5), 617–630.
- Global Centroid Moment Tensor (2022). Global CMT catalog search. [2021–01–07]. <https://www.globalcmt.org/CMTsearch.html>.
- He, W. G., Liu, B. C., Yuan, D. Y., & Yang, M. (2000). Research on slip rates of the Lenglongling active fault zone. *North-Western Seismological Journal*, 22(1), 90–97.
- Hu, C. Z., Yang, P. X., Li, Z. M., Huang, S. T., Zhao, Y., Chen, D., Xiong, W. R., & Chen, Y. Q. (2016). Seismogenic mechanism of the 21 January 2016 Menyuan, Qinghai $M_s6.4$ earthquake. *Chinese Journal of Geophysics*, 59(5), 1637–1646.
- Ji, L. Y., Liu, C. J., Xu, J., Liu, L., Long, F., & Zhang, Z. W. (2017). InSAR observation and inversion of the seismogenic fault for the 2017 Jiuzhaigou $M_s7.0$ earthquake in China. *Chinese Journal of Geophysics*, 60(10), 4069–4082.
- Li, Q., Jiang, Z. S., Wu, Y. Q., & Zhao, J. (2014). Inversion of locking and distribution of slip deficit in Haiyuan-Liupan fault zone using GPS data. *Geomatics and Information Science of Wuhan University*, 39(5), 575–580.
- Li, Y., Liu, X., Liu, X. K., Zhou, W., Zheng, Z., Zhang, L., Du, X., & Shen, X. (2016a). Activity analysis of faults around Qilianshan before the 2016 Menyuan $M_s6.4$ earthquake. *Journal of Geodesy and Geodynamics*, 36(4), 288–293.
- Li, Y., Shan, X., Qu, C., & Wang, Z. (2016b). Fault locking and slip rate deficit of the Haiyuan-Liupanshan fault zone in the northeastern margin of the Tibetan plateau. *Journal of Geodynamics*, 102, 47–57.
- Li, Y., Shan, X., Qu, C., Zhang, Y., Song, X., Jiang, Y., Zhang, G., Nocquet, J. M., Gong, W., Gan, W., & Wang, C. (2017). Elastic block and strain modeling of GPS data around the Haiyuan-Liupanshan fault, northeastern Tibetan plateau. *Journal of Asian Earth Sciences*, 150, 87–97.
- Li, Z. H., Han, B. Q., Liu, Z. J., Zhang, M. M., Yu, C., Chen, B., Liu, H. H., Du, J., Zhang, S. C., Zhu, W., Zhang, Q., & Peng, J.

- B. (2022). Source parameters and slip distributions of the 2016 and 2022 Menyuan, Qinghai earthquakes constrained by InSAR observations. *Geomatics and Information Science of Wuhan University*. <https://doi.org/10.1320/j.whugis20220037>
- Loveless, J., & Meade, B. (2011). Spatial correlation of interseismic coupling and coseismic rupture extent of the 2011 $M_w=9.0$ Tohokuoki earthquake. *Geophysical Research Letters*, 38(17), L17306.
- Mao, A., Harrison, C. G. A., & Dixon, T. H. (1999). Noise in GPS coordinate time series. *Journal of Geophysical Research*, 104(B2), 2797–2816.
- McCaffrey, R. (2002). Crustal block rotations and plate coupling. In: Stein, S., Freymueller, J.T. (Eds.), *Plate Boundary Zones*, AGU Geodynamics Series, 30, Washington D.C. pp. 101–122.
- McCaffrey, R. (2005). Block kinematics of the Pacific-North America plate boundary in the southwestern United States from inversion of GPS, seismological, and geologic data. *Journal of Geophysical Research*. <https://doi.org/10.1029/2004JB003307>
- Moreno, M., Rosenau, M., & Oncken, O. (2010). 2010 Maule earthquake slip correlates with pre-seismic locking of Andean subduction zone. *Nature*, 467(7312), 198–202.
- Okada, Y. (1992). Internal deformation due to shear and tensile faults in a half-space. *Bulletin of the Seismological Society of America*, 82(2), 1018–1040.
- Peng, Z., Liu-Zeng, J., Deng, Y., & Toda, S. (2022). Strong earthquake increases seismic hazard in Qinghai, China, Temblor. <https://doi.org/10.32858/temblor.230>
- Qu, C., Zhang, G., Shan, X., Zhang, G., Song, X., & Liu, Y. (2013). Coseismic deformation derived from analyses of C and L band SAR data and fault slip inversion of the Yushu $M_s7.1$ earthquake, China in 2010. *Tectonophysics*, 584, 119–128.
- Sandwell D, Mellors R, Tong X, Wei, M., & Wessel, P. (2011). GMTSAR: An InSAR processing system based on generic mapping tools. *Technical Report. Scripps Institution of Oceanography*, UC San Diego.
- Schurr, B., Asch, G., Hainzl, S., Bedford, J., Hoehner, A., Palo, M., Wang, R. J., Moreno, M., Bartsch, M., Zhang, Y., Oncken, O., Tilmann, F., Dahm, T., Victor, P., Barrientos, S., & Vilotte, J. (2014). Gradual unlocking of plate boundary controlled initiation of the 2014 Iquique earthquake. *Nature*, 512(7514), 299–302.
- Shan, X. J., Qu, C. Y., Gong, W. Y., Zhao, D. Z., Zhang, F. Y., Zhang, G. H., Song, X. G., Liu, Y. H., & Zhang, G. F. (2017). Coseismic deformation field of the Jiuzhaigou $M_s7.0$ earthquake from Sentinel-1A InSAR data and fault slip inversion. *Chinese Journal of Geophysics*, 60(12), 4527–4536.
- USGS (2022). USGS CMT catalog. [2022–01–07]. <https://earthquake.usgs.gov/earthquakes/eventpage/us7000g9zq/moment-tensor>
- Wang, R. Jt., Motagh, M. & Walter, T. R. (2008). Inversion of slip distribution from seismic deformation data by a Sensitivity Based Iterative Fitting (SBIF) method. //EGU General Assembly 2008. Vienna, Austria: EGU.
- Wang, M., & Shen, Z. K. (2020). Present day crustal deformation of continental China derived from GPS and its tectonic implications. *Journal of Geophysical Research: Solid Earth*, 125(2), e2019JB018774.
- Wang, H., Ge, L., Xu, C., & Du, Z. (2007). 3-D coseismic displacement field of the 2005 Kashmir earthquake inferred from satellite radar imagery. *Earth, Planets and Space*, 59, 343–349.
- Wang, H., Liu, M., Cao, J., Shen, X., & Zhang, G. (2011). Slip rates and seismic moment deficits on major active faults in mainland China. *Journal of Geophysical Research Solid Earth*. <https://doi.org/10.1029/2010JB007821>
- Wang, H., Liu-Zeng, J., Ng, A. H. M., Ge, L., Javed, F., Long, F., Aoudia, A., Feng, J., & Shao, Z. (2017). Sentinel-1 observations of the 2016 Menyuan earthquake: A buried reverse event linked to the left-lateral Haiyuan fault. *International Journal of Applied Earth Observation and Geoinformation*, 61, 14–21.
- Wang, Q., Niu, F., Gao, Y., & Chen, Y. (2016). Crustal structure and deformation beneath the NE margin of the Tibetan plateau constrained by teleseismic receiver function data. *Geophysical Journal International*, 204(1), 167–179.
- Wang, X. S., Fang, J., & Hsu, H. T. (2013). 3D density structure of lithosphere beneath northeastern margin of the Tibetan Plateau. *Chinese Journal of Geophysics*, 56(11), 3770–3778.
- Wu, Y., Jiang, Z., Liang, H., Chang, L., Chen, C., Zhu, S., Zhao, J., & Du, J. (2016). Coseismic deformations of the 2015 M_w 7.8 Gorkha earthquake and pre-seismic strain accumulation in the Himalayan tectonic belt and Tibetan plateau. *Tectonophysics*, 670, 144–154.
- Wu, Y., Jiang, Z., Pang, Y., & Chen, C. (2021). Statistical correlation of seismicity and geodetic strain rate in the Chinese mainland. *Seismological Research Letters*, 93(1), 268–276.
- Wu, Y. Q., Jiang, Z. S., Wang, M., Che, S., Liao, H., Li, Q., Li, P., Yang, Y. L., Xiang, H. P., Shao, Z. G., Wang, W. X., Wei, W. X., & Liu, X. X. (2013). Preliminary results of the co-seismic displacement and pre-seismic strain accumulation of the Lushan $M_s7.0$ earthquake reflected by the GPS surveying. *Chinese Science Bulletin*, 58(28–29), 1910–1916.
- Wu, Y., Jiang, Z., Yang, G., Fang, Y., & Wang, X. (2009). The application and method of GPS strain calculation in whole mode using least square collocation in sphere surface. *Chinese Journal of Geophysics*, 52(7), 1707–1724.
- Wu, Y., Jiang, Z., Yang, G., Wei, W., & Liu, X. (2011). Comparison of GPS strain rate computing methods and their reliability. *Geophysical Journal International*, 185(2), 703–717.
- Wu, Y. Q., Jiang, Z. S., Zhao, J., Liu, X. X., Wei, W. X., Liu, Q., Li, Q., Zou, Z. Y., & Zhang, L. (2015). Crustal deformation before the 2008 Wenchuan $M_s8.0$ earthquake studied using GPS data. *Journal of Geodynamics*, 85, 11–23.
- Xu, X., Sandwell, D. T., Tymofeyeva, E., Gonzalez-Ortega, A., & Tong, X. (2017). Tectonic and anthropogenic deformation at the Cerro Prieto geothermal step-over revealed by Sentinel-1A InSAR. *IEEE Transactions on Geoscience and Remote Sensing*, 55, 5284–5292.
- Yang, H., Wang, D., Guo, R., Xie, M., Zang, Y., Wang, Y., Yao, Q., Cheng, C., An, Y., & Zhang, Y. (2022). Rapid report of the 8 January 2022 $M_s6.9$ Menyuan earthquake, Qinghai, China. *Earthquake Research Advances*. <https://doi.org/10.1016/j.eqrea.2022.100113>
- Yuan, D. Y. (2022). Qinghai Menyuan $M6.9$ earthquake site inspection results released. <https://t.ynet.cn/baijia/32080013.html>. (Accessed 18 January 2022)
- Yuan, D. Y., Zhang, P. Z., Liu, B. C., Gan, W. J., Mao, F. Y., Wang, Z. C., Zheng, W. J., & Guo, H. (2004). Geometrical imagery and tectonic transformation of late quaternary active tectonics in Northeastern margin of Qinghai-Xizang plateau. *Acta Geologica Sinica*, 78(2), 270–278.

Zhao, J., Niu, A. F., Li, Q., & Yuan, Z. Y. (2016). Study on dynamic characteristics of fault locking and fault slip deficit in the faults around the Longxi block. *Journal of Seismological Research*, 39(3), 351–358.

Zhao, J., Ren, J., Liu, J., Jiang, Z., Liu, X., Liang, H., Niu, A., Yue, C., & Yuan, Z. (2020). Coupling fraction and relocking process of the Longmenshan fault zone following the 2008 M_w 7.9 Wenchuan earthquake. *Journal of Geodynamics*, 137, 101730.

(Received February 27, 2022, revised August 2, 2022, accepted August 4, 2022, Published online August 18, 2022)